RESEARCH PAPER

PCCP
www.rsc.org/pccp

The heterogeneous chemical kinetics of NO_3 on atmospheric mineral dust surrogates

Federico Karagulian and Michel J. Rossi*

Laboratoire de Pollution Atmosphérique et Sol (LPAS), Ecole Polytechnique Fédérale de Lausanne (EPFL), Lausanne, CH-1015, Switzerland. E-mail: michel.rossi@epfl.ch or mj.rossi@bluemail.ch.

Received 12th May 2005, Accepted 13th July 2005
First published as an Advance Article on the web 1st August 2005

Uptake experiments of NO_3 on mineral dust powder were carried out under continuous molecular flow conditions at 298 ± 2 K using the thermal decomposition of N_2O_5 as NO_3 source. *In situ* laser detection using resonance enhanced multiphoton ionization (REMPI) to specifically detect NO_2 and NO in the presence of N_2O_5, NO_3 and HNO_3 was employed in addition to beam-sampling mass spectrometry. At $[NO_3] = (7.0 \pm 1.0) \times 10^{11}$ cm^{-3} we found a steady state uptake coefficient γ_{ss} ranging from $(3.4 \pm 1.6) \times 10^{-2}$ for natural limestone to (0.12 ± 0.08) for Saharan Dust with γ_{ss} decreasing as $[NO_3]$ increased. NO_3 adsorbed on mineral dust leads to uptake of NO_2 in an Eley–Rideal mechanism that usually is not taken up in the absence of NO_3. The disappearance of NO_3 was in part accompanied by the formation of N_2O_5 and HNO_3 in the presence of NO_2. NO_3 uptake performed on small amounts of Kaolinite and $CaCO_3$ leads to formation of some N_2O_5 according to $NO_{3(ads)} + NO_{2(g)} \rightarrow N_2O_{5(ads)} \rightarrow N_2O_{5(g)}$. Slow formation of gas phase HNO_3 on Kaolinite, $CaCO_3$, Arizona Test Dust and natural limestone has also been observed and is clearly related to the presence of adsorbed water involved in the heterogeneous hydrolysis of $N_2O_{5(ads)}$.

1. Introduction

Atmospheric chemistry is driven by reactions of free radicals owing to their reactivity with many trace gases. In addition to OH, HO_2 and O_3 that exert their oxidizing potential in the atmosphere under photolytic conditions, the nitrate free radical, NO_3,[1] is an important atmospheric oxidizing agent in the nighttime atmosphere whose reactivity with unsaturated biogenic hydrocarbons as well as with aldehydes and ketones[2] is comparable to the reactivity of the hydroxyl free radical in the daytime atmosphere. Together with O_3, nitrate radical represents a significant part of the oxidation potential of the atmosphere at night. Under conditions of the simultaneous presence of NO_x, O_3 and reactive organic gases in the same air mass, NO_3 is responsible for the nighttime formation of organic peroxy free radicals that are precursors to tropospheric O_3. NO_3 is thereby involved in the rate-limiting step of either H abstraction from or addition to an olefinic double bond.

Specifically, the presence of NO_3 that rapidly undergoes photolysis during the day, has several important consequences for tropospheric chemistry. It controls reactive nitrogen, NO_y, at night by forming N_2O_5 which undergoes heterogeneous hydrolysis to HNO_3, an important daytime reservoir compound for NO_2. The fast radical recombination reaction between NO_3 and NO_2 leading to N_2O_5 is the only known source for HNO_3 at nighttime. NO_3 also acts as an initiator for the formation of non-photolytic OH free radicals at night through reaction of HO_2 with NO, thereby starting oxidation chain reactions of reactive organic gases. Lastly, NO_3 may form peroxyacetyl and other organic nitrates that may also act as temporary NO_x reservoirs.[2,3]

Atmospheric nigthttime concentrations of NO_3 reach values of up to 4.0×10^7 molecule cm^{-3} in the stratosphere[4] and 2.0×10^9 molecule cm^{-3} in the troposphere.[5] Despite these significant concentrations only a few studies of the heterogeneous reactions of the nitrate radical have been performed,[6–10] none so far on mineral dust. The present study intends to fill this gap by studying the NO_3 uptake on mineral dust and some of its surrogates in order to obtain a value for the uptake coefficient γ for NO_3 that may be included in the global modeling of heterogeneous chemistry on mineral dust aerosols.

Mineral dust aerosols are recognized to have an important influence on atmospheric composition,[11,12] both because they provide reactive surfaces for heterogeneous chemical reactions and affect the solar flux through scattering and absorption of radiation.[13–16] Mineral dust consists of fine particles of crustal origin generated by wind erosion whose main constituents are mostly silica and silicate minerals. Recent modeling studies estimate yearly emission fluxes between 800 and 1500 Tg yr^{-1} [17] whipped up from approximately 33% of the global land surface that is arid and therefore may be a potential source region for atmospheric mineral dust aerosol.[18,19] Globally, the most important minerals of the clay fraction (<2 μm) transported in dust storms are illite, kaolinite, chlorite and montmorillonite/smecite,[20] whereas coarse particles mainly consist of quartz, feldspar and carbonates.[21] The presence of mineral dust aerosols represents a direct climate forcing due to their effect on scattering and absorption of solar radiation and therefore affect the photochemical reaction rates as well.[13–16] Together with HNO_3 and N_2O_5, NO_3 contributes to the formation of particulate nitrate on the dust particles by surface processes in the troposphere.[22]

Field observations,[23,24] laboratory[25–29] and modelling studies have firmly established the interaction of trace gases with mineral dust aerosol as well as the quantitative impact of the latter on the composition of the atmosphere. There is no study at this time that directly proposes the uptake of NO_3 on mineral dust surfaces from measurements of the nitrate radical in the lower troposphere despite field measurements that report NO_3 concentrations[30] and mixing ratios[31] as a function of meteorological data. Box, regional and global scale models have gauged the importance of dust on both the photochemical rates of oxidant formation as well as the loss of trace gases regarding atmospheric composition.[22,32–35] The comparison of

DOI: 10.1039/b506750m

the global scale models of Bian and Zender[34] with the one presented by Bauer *et al.*[35] reveals significant quantitative differences of the effect of mineral dust on O_3 and several important trace gases such as HNO_3, N_2O_5 and H_2O_2. However, both studies agree that the direct interaction of O_3 with mineral dust is of minor importance, whereas the uptake of its precursor HNO_3 is responsible for most of the ozone decrease in the areas affected by dust. It is difficult to quantitatively compare the results of Bian and Zender with Bauer *et al.* because the uptake coefficient γ for HNO_3 on global mineral dust is a factor of 100 lower whereas γ for NO_3 is a factor of 33 larger in the former. This reflects both the uncertainty of past measurements as well as the absence of experimental information that is replaced by guesswork such as in the case of NO_3. We have therefore embarked on a laboratory program to measure some of the heterogeneous reactions involving NO_3 (this work) and N_2O_5 likely to be important in global mineral dust studies.

2. Experimental aspects

Experiments have been performed at 298 ± 2 K using a very low pressure Knudsen flow reactor, described in detail in the Appendix and elsewhere (Fig. 1).[36] In order to unambiguously monitor the concentration of NO and NO_2, resonance enhanced multiphoton ionization (REMPI) was employed *in situ* as part of a multi-diagnostic experimental technique in addition to molecular beam-sampling electron-impact mass spectrometry (MS) coupled to phase-sensitive detection. The experimental REMPI set up used in the present work is described in detail in the Appendix and, in conjunction with MS, allows the unambiguous detection of a mixture of the following gases important in the present work: NO_3, NO_2, NO, HNO_3 and N_2O_5. The two-color REMPI detection will be presented in detail in the Appendix.

The gases under study were introduced into the Knudsen reactor from the gas handling system across a capillary. An isolation plunger allows the separation of the reactive surface of interest from the reactor volume. The gases leave the Knudsen reactor through an escape orifice whose variable diameter in the range 1–14 mm determines the residence time ($\tau_g = 1/k_{esc}$) and molecular concentration at a measured flow rate F_0^M.

MS provides a measurement of the species concentration [M] after establishment of a calibration factor using measured flow rates F_0^M of stable gases effusing out of the reactor following eqn. (E.1):

$$F_0^M = I_0^M C_{cal(M)} \qquad (E.1)$$

where I_0^M is the MS signal and $C_{cal(M)}$ is a calibration factor for the species M of interest whose value depends on the MS instrumental parameters. The instantaneous concentration $[M]_{MS} = N/V_{cell}$ of the total number of molecules in the reactor is related to the flow F_0^M of molecules leaving the reactor according to eqn. (E.2):

$$[M]_{MS} = \frac{F_0^M}{k_{esc} V_{cell}} \qquad (E.2)$$

The rate constant for the effusive loss k_{esc} is given by the kinetic theory of gases and was routinely measured for each compound. Owing to the fact that the loss of the NO_3 free radical includes both physical, that is effusion, and chemical wall-loss processes, the usual algebra for the retrieval of γ is slightly more complex as explained below and in Table 1. The characteristic parameters and relevant kinetic expressions used in this work are given in Table 1.

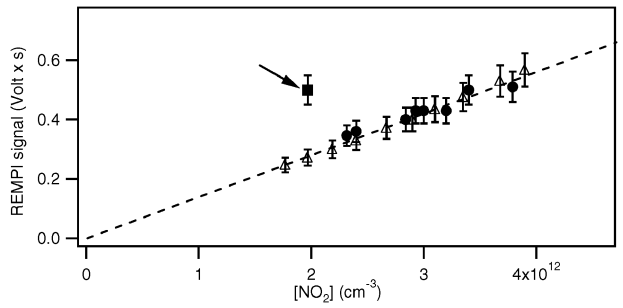

Fig. 1 REMPI signal at $\lambda_{NO} = 452.6$ nm as a function of $[NO_2]$ for a pure NO_2 flow (open triangles) plotted together with the signal resulting from a mixture of NO_2 and NO_3 flowing out of the hot NO_3 source (filled circles). The point marked with the arrow represents the hypothetical REMPI signal at $\lambda_{NO} = 452.6$ nm if we have 10% of NO in a mixture of NO_2 and NO_3 at $[NO_3] = 2.0 \times 10^{12}$ cm^{-3}. The absolute concentration of NO_2 and NO_3 have been separately determined using REMPI detection at $\lambda_{NO_2} = 511$ nm and MS at m/z 62, respectively, (orifice diameter = 8 mm).

2.1 Sample preparation

The used samples are the following: Kaolinite, poorly ordered (KGa-2, Warren County, Georgia, USA), $CaCO_3$ (Fluka), natural limestone (Transmat SA, La Sarraz, Switzerland), Arizona Medium Test Dust (Powder Technology Incorporated, Burnsville MN), Saharan Dust collected from deposits on the Cape Verde Islands and Molecular sieve (Fluka). Two kinds of sample holders were used: one consisted of a TEFLON® coated Pyrex holder having an available sample surface of 19.6 cm^2, the other consisted of an internal reduction piece made out of DELRIN®, an acetal resin, leading to a sample surface of 4.9 cm^2. DELRIN® showed a modest reactivity towards uptake of NO_3 resulting in $\gamma_{DELRIN} = 8.2 \times 10^{-3}$. We discovered during the study that DELRIN® is less porous for small molecules such as H_2O and less sticky for HNO_3 with respect to TEFLON®. As a consequence, we applied the appropriate corrections to all uptake measurements. In order to probe diffusion effects of NO_3 inside bulk powders, several additional reference experiments were carried out. Glass optical flats of 19.6 cm^2 were sprayed with a mineral dust suspension in methanol or water in order to obtain a sample whose total exposed surface is equal to the sample holder. Typically, 5–20 mg of powder can be deposited onto the glass support to full coverage judged by eye and resulting in an average thickness of less than 4 μm. The purpose of these experiments was to obtain samples consisting of a few monolayers ever so poorly characterized in order to probe the mass dependence of NO_3 uptake. Most of the experiments have been carried out with gram quantities rather than mg. Uptake experiments have been carried out using mineral dust samples that were pumped for half an hour to less than 10^{-7} Torr at $T = 294$ K after which no H_2O desorption has been observed.

2.2 NO_3 source

NO_3 was generated by thermal decomposition of N_2O_5 inside a 6 cm long hot glass tube of 0.6 cm diameter that was externally heated to 530 K using NiCr wire thereby approaching 100% decomposition of N_2O_5 under the chosen experimental conditions according to reaction (1):

$$N_2O_5 \rightarrow NO_2 + NO_3 \qquad (1)$$

N_2O_5 flow rates were on the order of 10^{16} molecule s^{-1} and were determined by measuring the pressure drop $\Delta P/\Delta t$ as a function of time when N_2O_5 flowed out of a calibrated volume. N_2O_5 was synthesized off-line by the oxidation of NO_2 with excess ozone. The O_3/O_2 mixture that evolves from an ozonizer is passed through a P_2O_5 trap in order to eliminate residual moisture before being mixed with dried NO_2. N_2O_5 is collected in a methanol/dry-ice bath at 195 K and is subsequently analyzed for purity by MS at m/z 46 and m/z 30.

Table 1 Characteristic parameters and relevant kinetic expressions

Definition	Value
Reactor volume, V	2000 cm^3
Reactor surface area, A_r	1500 cm^2
Sample surface area, A_s	19.6 cm^2 (TEFLON holder), 4.9 cm^2 (DELRIN holder)
Collision frequency ω (nominal) of NO_3 with A_s	$\omega = 1.81(T/M)^{1/2}A_s\ s^{-1}$
Orifice diameters (nominal)	4, 8 and 14 mm
k_{esc} (experimentally determined values for nominal orifice diameters using an inert gas)[a]	$0.25(T/M)^{1/2}\ s^{-1}$ for 4 mm orifice
	$0.8(T/M)^{1/2}\ s^{-1}$ for 8 mm orifice
	$1.9(T/M)^{1/2}\ s^{-1}$ for 14 mm orifice
Rate constant of chemical first-order wall loss of free radical in the absence of heterogeneous reaction with the sample	$k_{dec}\ s^{-1}$
Rate constant for total loss of free radical	$k' = k_{esc} + k_{dec}\ s^{-1}$
Observed rate constant for heterogeneous reaction from steady state experiments, S_i = initial MS-signal; S_f = final MS-signal	$k_{obs} = (S_i/S_f - 1)k'\ s^{-1}$
Observed uptake coefficient	$\gamma_{obs} = k_{obs}/\omega$

[a] T/K, M/g.

NO_3 was monitored using mass spectrometry at $m/z = 62$ (NO_3^+), HNO_3 at $m/z = 63$ (HNO_3^+), NO and NO_2 by REMPI detection at $\lambda_{NO} = 452.6$ nm and $\lambda_{NO_2} = 511$ nm, respectively (see Appendix). N_2O_5 did not have a measurable parent peak under our experimental conditions; the most intense peak was its fragment NO_2^+ at m/z 46. Both N_2O_5 and HNO_3 did not show any measurable contribution at m/z 62 in reference experiments such that these two species did not interfere with the MS detection of NO_3. In reference experiments of pure N_2O_5 m/z 62 was 0.01% of the base peak at m/z 46.

Hydrolysis of N_2O_5 may occur on internal surfaces of the inlet line before admission into the hot glass capillary generating HNO_3 as an impurity on the order of 10 to 15%. HNO_3 does not thermally decompose inside the hot glass tube of the NO_3 source because we did not observe any change in the MS signal amplitude at m/z 63 when increasing the source temperature to 530 K. In addition, using pure NO_2-free HNO_3 flowing through the hot NO_3 source and using REMPI detection at $\lambda_{NO_2} = 511$ nm no REMPI signal of NO_2 from potential heterogeneous decomposition of HNO_3 on the hot walls of the source vessel was detected. We attribute this apparent resistance to decomposition to the small HNO_3 residence time of approximately 400 μs in the hot glass tube.

2.3 Calibration of NO_3 and secondary reactions in the NO_3 source

The NO_3 concentration has been determined by titration with NO according to reaction (2) where the end point has been detected by monitoring the additional NO_2 at excess NO:

$$NO_3 + NO \rightarrow 2NO_2 \qquad (2)$$

With a NO concentration of approximately 1.0×10^{12} cm^{-3} the reaction is fast enough to convert more than 90% of the NO_3 inside the reactor using $k_{(298\ K)} = 2.6 \times 10^{-11}$ cm^3 $molecule^{-1}$ s^{-1}. The titration experiment at $T = 298$ K resulted in a yield of 143 ± 29% NO_2 and 54 ± 18% NO_3 (error represents one standard deviation) with respect to N_2O_5 decomposed. The deviation from the expected 100% yield for both NO_2 and NO_3 indicates a fast secondary decomposition reaction of NO_3 into NO_2 or NO within the hot glass tube of the source.[37]

Both REMPI detection at $\lambda_{NO_2} = 511$ nm (NO_2) and MS detection at m/z 62 (NO_3) allowed us to verify the mass balance of NO_3 with N_2O_5 and to conclude that the thermal decomposition of N_2O_5 is complete and that therefore no N_2O_5 is present in the mixture of NO_3 and NO_2 coming from the NO_3 source.

Possible candidates for products resulting from wall decomposition of NO_3 are NO_2 and NO according to reactions (3) and (4):

$$NO_3 \rightarrow NO_2 + 1/2O_2,\ \Delta H_{r(gas)}{}^0 = -9.1\ kcal/mol \qquad (3)$$

$$NO_3 \rightarrow NO + O_2,\ \Delta H_{r(gas)}{}^0 = +4.6\ kcal/mol \qquad (4)$$

In order to find the products of the wall decomposition of NO_3 without ambiguity we performed an ancillary experiment taking advantage of simultaneous REMPI detection of NO and NO_2 at $\lambda_{NO} = 452.6$ nm, the primary wavelength for NO detection (see Appendix). In addition to NO, NO_2 is also detected at this wavelength owing to concomitant photolysis of NO_2 to NO and subsequent REMPI detection of NO. As displayed in Fig. 1, the ion yield for REMPI detection at $\lambda_{NO} = 452.6$ nm has been plotted as a function of [NO_2] originating from a pure NO_2 flow (open triangles) together with the ion yield of [NO_2] from a mixture of NO_2 and NO_3 originating from the hot NO_3 source (filled circles). Both [NO_2] and [NO_3] in the mixture have previously been independently determined by using REMPI detection at $\lambda_{NO_2} = 511$ nm for [NO_2] and the MS signal I^{62} at m/z 62 for [NO_3], respectively. Based on Fig. 1, we conclude that reaction (3) is the reason for the excess of NO_2 over NO_3 (see above) because it shows the complete absence of NO detected at $\lambda_{NO} = 452.6$ nm. The fact that the REMPI signal of the pure NO_2 reference gas coincides with the mixture flowing out of the NO_3 source leads to the conclusion the NO must be absent from the mixture which excludes reaction (4) as a candidate for wall decomposition of NO_3. Fig. 1 shows the expected REMPI signal of NO_2 containing 10% NO which is 50% larger compared to pure NO_2 owing to the four-fold higher sensitivity of NO *vs.* NO_2 at $\lambda_{NO} = 452.6$ nm as shown in the Appendix. Fig. 1 also shows that a 5% impurity of NO in NO_2 may be detected using REMPI. Potential NO that is formed heterogeneously following reaction (4) can only be partially titrated *via* reaction (2) because the titration rate is too slow in the absence of an excess of [NO_3]. This would lead to some NO that should therefore be detectable if formed in reaction (4) owing to the absence of NO. We therefore exclude the heterogeneous decomposition of NO_3 according to reaction (4) with high confidence.

We were unable to measure any change in the O_2 signal following reaction (3) because molecular oxygen is present as a background gas in our detection chamber owing to small leaks. It was therefore impossible to separate the small expected O_2 contribution due to the NO_3 decomposition from the O_2

Table 2 Comparison of calculated rate constant for effusion, k_{esc}, and measured loss rate constant of NO_3, $k' = k_{esc} + k_{dec}$, in Knudsen cell flow reactor of differing orifice diameters

∅ escape orifice/mm	Calculated k_{esc}/s^{-1}	Measured k'/s^{-1}	k_{dec}/s^{-1}
14	4.15	5.0	0.85
8	1.74	2.3	0.56
4	0.54	0.9	0.36

background. Molecular oxygen is the expected stable NO_3 decomposition product from both reaction pathways, reactions (3) and (4).

2.4 Wall loss of NO_3 in the Knudsen flow reactor

NO_3 itself was also subject to unspecified wall-loss in the Knudsen reactor as the measured rate of loss was consistently higher than the expected or calculated value (see Table 2). This indicated that a competing NO_3 loss process with a rate constant k_{dec} adds to the expected, that is calculated, rate constant for effusion k_{esc} based on the measured effusion rate of non-reactive gases such as N_2, Ar, CO_2 and SF_6. The relative concentration of NO_3 is decreasing with decreasing orifice size because it undergoes wall loss with increasing residence time in the Knudsen reactor. Lower signals at smaller orifices, that is, at longer residence time in the reactor, indicate a loss process for NO_3.[38] The measured first-order rate of loss given by k' of NO_3 at a given escape orifice size of the reactor is based on the observed single-exponential decay of NO_3. It may actually be expressed as the sum of two components, namely k_{esc} and k_{dec}, representing escape, that is physical loss, and chemical loss, respectively:

$$k' = k_{esc} + k_{dec} \qquad \text{(E.3)}$$

The measurement of k' at three different aperture sizes (Table 2) enabled the determination of $k_{dec} = 0.60 \pm 0.27\ s^{-1}$. The additional loss process of NO_3 was found to be first order with respect to NO_3 and constant over the course of all performed experiments. In this work every measurement of k_{obs} has been performed using k' instead of $k_{esc.}$ We therefore determined the observed rate constant k_{obs} taking $k' = k_{esc}$ (theoretical value) $+ k_{dec}$ as an effective loss process instead of k_{esc} resulting in the following equation:

$$k_{obs} = \left(\frac{[NO_3]_0}{[NO_3]_r} - 1\right)(k_{esc} + k_{dec}) \qquad \text{(E.4)}$$

where $[NO_3]_0$ and $[NO_3]_r$ are the NO_3 concentrations calculated from MS signal $I^{62(NO_3)}$ at m/z 62 before and during reaction, respectively.

2.5 Determination of the uptake coefficient

In the Knudsen flow reactor, reactant gas molecules either exit through an aperture into the pumping chamber or are lost on the reactive surface. A net observed uptake coefficient for NO_3, γ_{obs}, given by the following expression and is only valid if the rate law for uptake is first order in NO_3:

$$\gamma_{obs} = \frac{k_{obs}}{\omega} \qquad \text{(E.5)}$$

In eqn (E.5) k_{obs} is the pseudo-first-order rate constant at steady state conditions, ω the collision frequency of a molecule with the reactive surface area A_s of the sample defined as $\omega = \frac{\bar{c}}{4V_{cell}} A_s$ where $\bar{c}$ is the mean velocity and V_{cell} the volume of the reactor. In our data analysis, γ_{obs} was calculated using the geometric surface area of the sample holder which will be justified below based on additional reference experiments. In the present work the observed uptake coefficient γ_{obs} became γ_{ss}, when the uptake of NO_3 monitored at m/z 62 clearly reached steady state at 400 s of exposure time whereas γ_0 equals γ_{obs} at $t = 0$ s, *i.e.* immediately after lifting the plunger. Upon increasing the exposure time by a factor of two, γ_{ss} did not change significantly.

Continuous flow uptake experiments were carried out at ambient temperature (298 ± 2 K) under molecular flow conditions. The concentration of NO_3 inside the Knudsen reactor was kept constant at $(7.0 \pm 1.0) \times 10^{11}$ and $(4.0 \pm 1.0) \times 10^{12}$ cm^{-3} for low and high $[NO_3]$ experiments, respectively. The associated $[NO_2]$ determined by REMPI was $(1.7 \pm 1.0) \times 10^{12}$ cm^{-3} for $[NO_3] = (7.0 \pm 1.0) \times 10^{11}$ cm^{-3} and $(7.3 \pm 2.0) \times 10^{12}$ cm^{-3} for $[NO_3] = (4.0 \pm 1.0) \times 10^{12}$ cm^{-3}. In ancillary experiments, it was found that NO_2 only interacted with Saharan Dust whereas all other examined surrogate dust samples did not show any reactivity towards NO_2 under the selected experimental conditions.

2.6 Product study

The mass spectra of the species involved in the NO_3 source share common fragment peaks when using MS detection. The main common fragment and molecular ion peaks for NO_3, N_2O_5, NO_2, NO and HNO_3 are m/z 46 and 30. The REMPI detection of NO_2 allowed us to subtract with great accuracy the contribution of NO_2 to the total MS signal $I_0{}^{46}$ at m/z 46 originating from the source.

As indicated above, we observed that the NO_3 source contains HNO_3 as an impurity that contributes to the total MS signal at m/z 46. Fortunately, at the present experimental conditions HNO_3 has a measurable, albeit low intensity, parent peak at m/z 63. In order to evaluate the contribution of HNO_3 at m/z 63 and m/z 46, we have analyzed the MS spectrum of pure HNO_3 which has been prepared from a mixture of liquid HNO_3 (90%, Fluka AG) and H_2SO_4 (98%, Fluka AG) in a ratio of 1:3 v/v. Subsequently, we bubbled N_2 for about 10 minutes under reduced pressure through the mixture in order to rid the solution of trace amounts of NO_2. The base and parent peak of HNO_3 are at m/z 46 ($NO_2{}^+$) and m/z 63 ($HNO_3{}^+$), respectively. In addition, we did not observe any NO_2 impurity in HNO_3 following REMPI detection at $\lambda_{NO_2} =$ 511 nm, that is specific for NO_2. Using the detailed mass spectrum of pure HNO_3 we have accurately determined the effective contribution of HNO_3 at m/z 46 by using the measured fragmentation pattern $f = \frac{I_0^{46(HNO_3)}}{I_0^{63(HNO_3)}} = 52 \pm 8$. The absolute NO_2 concentration $[NO_2]_{0(REMPI)}$ originating from the NO_3 source has been determined by means of REMPI detection according to eqn (E.A1) (Appendix). In order to calculate its corresponding MS signal contribution $I_{0(REMPI)}^{46(NO_2)}$ at m/z 46, we used the following equation:

$$I_{0(REMPI)}^{46(NO_2)} = \frac{[NO_2]_{0(REMPI)} k_{esc(NO_2)} V_{cell}}{C_{cal(NO_2)}} \qquad \text{(E.6)}$$

where $C_{cal(NO_2)}$ is the NO_2 calibration factor obtained from eqn (E.1) for pure NO_2 and $k_{esc(NO_2)}$ is its effusive loss rate constant. Eqn. (E.6) allows one to calculate the fraction of the MS signal at m/z 46 owing to the presence of NO_2 using the measured REMPI signal for NO_2 to establish its absolute concentration. No molecular species including NO_3 other than NO_2 gives rise to a REMPI signal at $\lambda_{NO_2} = 511$ nm.

In the absence of any substrate, $I_{0(REMPI)}^{46(NO_2)}$ and $fI_0{}^{63(HNO_3)}$ have been subtracted from the total MS signal $I_0{}^{46}$ at m/z 46 in order to attribute the remaining signal to the $NO_2{}^+$ fragment of the electron-impact ionization of NO_3 once the absence of undissociated N_2O_5 from the NO_3 source was established:

$$I_0^{46(NO_3)} = I_0^{46} - I_{0(REMPI)}^{46(NO_2)} - fI_0^{63(HNO_3)} \qquad \text{(E.7)}$$

When the sample is exposed to the gases from the NO_3 source, NO_3 is taken up and reacts on the mineral dust surface resulting in a decrease of $[NO_3]$ which leads to a concomitant decrease of the MS signal I_r^{46} at m/z 46. As shown in previous studies on mineral dust,[27] HNO_3, present as an impurity, reacts on the dust surface without formation of volatile products that may contribute to the total MS signal I_r^{46}.

We have determined $r = \frac{I_0^{46(NO_3)}}{I_0^{62(NO_3)}} = 9.5 \pm 2.0$ as the ratio of the MS signal $I_0^{46(NO3)}$ at m/z 46 (NO_2^+) and $I_0^{62(NO_3)}$ at m/z 62 (NO_3^+) for NO_3 free radical.

As a result of the exposure of the sample to NO_3 we expect two possible reaction products: HNO_3 and/or N_2O_5. Under our experimental conditions HNO_3 may possibly be formed at high densities by heterogeneous recombination of NO_2 and NO_3 to N_2O_5 and subsequent heterogeneous hydrolysis. HNO_3 has in fact been observed at m/z 63 resulting from the interaction of NO_3 with excess NO_2 under the present experimental conditions. In order to find other possible reaction products contributing to an excess I_{exc}^{46} MS signal intensity at $m/z = 46$ not due to HNO_3, we have subtracted the following known contributions from the total MS signal I_r^{46}: (a) $I_{0(REMPI)}^{46(NO_2)}$ for NO_2, (b) $rI_r^{62(NO_3)}$ for NO_3, (c) $fI_r^{63(HNO_3)}$ for the possible HNO_3 formation during the reaction. The final expression for the residual amplitude I_{exc}^{46} resulted from the following equation:

$$I_{exc}^{46} = I_r^{46} - I_{r(REMPI)}^{46(NO_2)} - rI_r^{62(NO_3)} - fI_r^{63(HNO_3)} \qquad (E.8)$$

The resulting residual MS signal from eqn. (E.8) is related to reaction products owing to the heterogeneous interaction of NO_3 with the exposed surface of the sample. It is reasonable to expect that N_2O_5 may be the only reaction product contributing to m/z 46 as will be discussed below.

2.7 Experimental uncertainties

The uncertainties for NO_3 and HNO_3 were determined from the signal to noise ratio of the MS signal at m/z 62 and m/z 63 and were estimated at ±15% and ±20%.

The uncertainties for [NO] and $[NO_2]$ were estimated at ±15% and ±10%, respectively. They have been determined from the signal to noise ratio of the REMPI signal at $\lambda_{NO} =$ 452.6 nm and $\lambda_{NO_2} = 511$ nm, respectively.

Based on the uncertainty of f (±8%) and on a typical uncertainty of ±10% of the REMPI signal the resulting overall uncertainty for $I_0^{46(NO_3)}$ is estimated at ±18%. On the other hand, the composite uncertainty of I_{exc}^{46} is evaluated at ±45% based on the relative uncertainties of 10, 15 and 20% for the REMPI signal of NO_2 as well as the MS signal contributions of NO_3 and HNO_3 to m/z 46, respectively. Therefore, N_2O_5 will be the only species that will be measured at an appreciable uncertainty of ±45% owing to the numerous subtracted contributions at m/z 46.

3. Uptake of NO_3: results and discussion

Typical raw data of an uptake experiment of NO_3 on 2 g of $CaCO_3$ are shown in Fig. 2a. After a steady flow of NO_3 had been established, the isolation plunger is lifted at $t = 400$ s and the substrate is exposed to the NO_3 flow. Because of the uptake of NO_3 on $CaCO_3$, the number of molecules effusing through the escape orifice into the MS decreases immediately. In all the performed experiments, NO_3 adsorbed on available surface sites gave rise to uptake of NO_2 that stems from the thermal decomposition of N_2O_5 and NO_3 (reactions (1) and (3)). This leads to a net decrease of the REMPI signal for NO_2 at $\lambda_{NO_2} =$ 511 nm. As the exposure time increases, the MS signal at m/z 62 (curve (d), Fig. 2a) partially recovers, indicating a decrease in the rate of uptake of NO_3 presumably owing to a decrease of

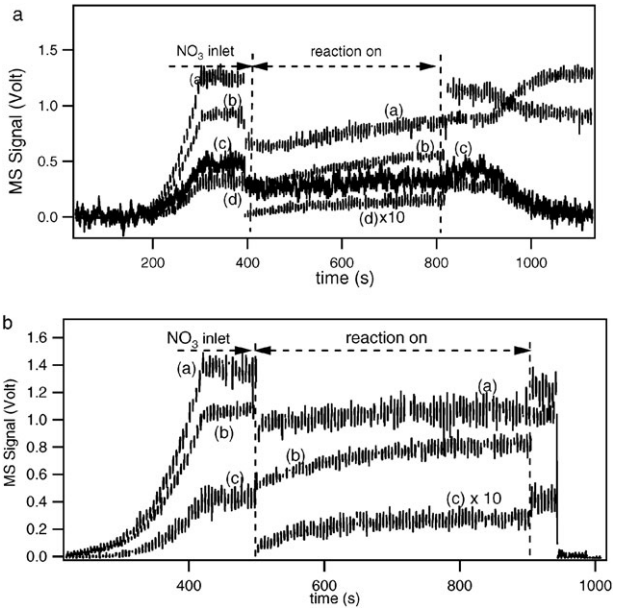

Fig. 2 (a) Typical Knudsen reactor experiment for NO_3 uptake on a sample of 2 g of $CaCO_3$ at $[NO_3] = (7.0 \pm 1.0) \times 10^{11}$ cm^{-3} (orifice diameter = 8 mm, $A_s = 19.6$ cm^2). Curves (a), (b) and (d) correspond to the raw MS signals monitored at m/z 30, m/z 46 and m/z 62, respectively. Curve (c) corresponds to the raw REMPI signal for NO_2 detection at $\lambda_{NO_2} = 511$ nm converted to a MS signal at m/z 46. Fig. 2b: Typical Knudsen reactor experiment for NO_3 uptake on a sample of 2 g of $CaCO_3$ at $[NO_3] = (7.0 \pm 1.0) \times 10^{11}$ cm^{-3} (orifice diameter = 14 mm, $A_s = 19.6$ cm^2). Curves (a), (b) and (c) correspond to the raw MS signals monitored at m/z 30, m/z 46 and m/z 62, respectively.

the number of available surface sites for reaction. This results in an apparent reduction of the uptake coefficient. At $t = 820$ s the sample compartment is sealed by lowering the plunger and the MS signal at m/z 62 returns to its initial value. Fig. 2b shows analogous results for the largest escape orifice leading to a larger rate of NO_3 uptake on solid $CaCO_3$. The lower concentration and the concomitant lower residence time τ_g of NO_3 in the reactor results in a lower degree of saturation and thus enhanced uptake.

In order to unravel whether or not the effective available surface area is influenced by the internal surface area formed by interstitial voids between individual dust particles, the mass dependence of the NO_3 uptake on Kaolinite was measured in the Knudsen flow reactor at ambient temperature and at $[NO_3] = (7.0 \pm 1.0) \times 10^{11}$ cm^{-3}. The mass of Kaolinite ranged from 5 mg to 1 g and the results are shown in Fig. 3. For the experiments performed at masses between 5 and 30 mg we used sprayed samples, whereas for masses between 110 mg and 1 g Kaolinite powder samples were used. Table 3 reports values of γ_{ss} using the geometric surface area of the sample holder that increase linearly with mass at low masses as displayed in Fig. 3. Samples of mass below 250 mg were considered part of this linear mass-dependent regime beyond which γ_{ss} converged to a limiting value of $\gamma_{ss} = 5.5 \times 10^{-2}$ corresponding to 4.5×10^{17} molecules of NO_3 taken up during a reaction time of 400 s. The significance of this number will be discussed below.

Increasing the sample mass beyond 250 mg at the intersection of the linear mass dependence b) of γ_{ss} in Fig. 3 with the horizontal line representing γ_{ss} had no effect on γ_{ss} as well as the amount of adsorbed NO_3 because apparently not the entire internal sample surface area is available for NO_3 adsorption. The limiting γ_{ss} value represents the maximum amount of NO_3 able to interact with Kaolinite powder within the NO_3 residence time owing to the inability of NO_3 to penetrate into the sample.

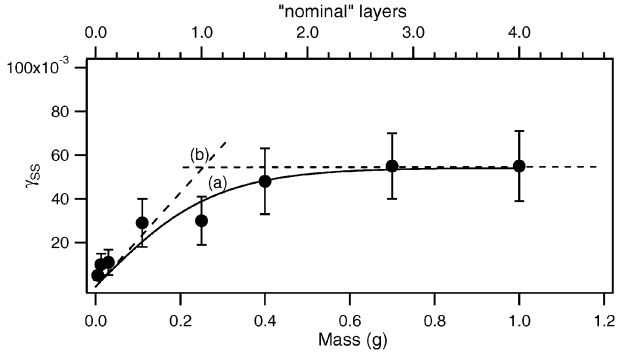

Fig. 3 Uptake of NO_3 on Kaolinite: dependence of the steady state uptake coefficient γ_{ss} on sample mass at $[NO_3] = (7.0 \pm 1.0) \times 10^{11}$ cm^{-3} (orifice diameter = 8 mm, $A_s = 19.6$ cm^2). The number of nominal layers is reported on the upper abscissa. Full circles: experimental values. Dependence (a): fit of the data using the pore diffusion model. Point (b): intersection of the linear and constant part of the curve which corresponds to the mass of one nominal layer of Kaolinite (see text).

In order to determine the number of layers, the total volume of Kaolinite powder was calculated from its true density $\rho_t = 2.3$ g/cm^3 and the mass of the sample spread out across the geometric area of the sample holder.

From the average particle size and the thickness of the sample we calculated the number of layers. The number of formal layers calculated for an average sample grain diameter of 1.0 μm is reported in Table 3. The typical grain diameter of 1.0 μm has been obtained from the manufacturer's undocumented specifications of the used Kaolinite powder. However, most mineral dust powders are porous materials and the microstructure of the dust substrate is composed of clusters of random distribution with interstitial voids between them. Therefore it is more reasonable to take into account a grain size diameter that is much larger than 1.0 μm as suggested by electron microscopy (SEM) of similar material where characteristic grain diameters are in the tens of micrometres (© OMNI Laboratories, Inc).

Fig. 3 shows that a mass of 250 mg corresponds to one nominal layer of 50 μm diameter Kaolinite spread out over the geometric surface of the sample holder (19.6 cm^2). Thus, one nominal layer of Kaolinite will contain closely packed spheres of "effective" grain diameter of 50 μm knowing full well that the sample in reality is multidisperse and structurally heterogeneous. Therefore, the linear mass-dependent portion of γ_{ss} *vs.* mass corresponds to a sample holder partially covered with 50 μm diameter Kaolinite particles which is the structural model we adopt in this work.

The use of the BET surface area and the pore diffusion theory (KLM)[39] would substantially underestimate the true uptake coefficient approximately between a factor of 10^2 to 10^3. The application of the pore diffusion theory results in $\gamma_{pd} = 1.7 \times 10^{-5}$, using a tortuosity factor $\tau = 2$ for a grain size of 1 μm (curve (a), Fig. 3). The assumption that NO_3 interacts with the total BET internal surface leads to $\gamma_{BET} = 2.0 \times 10^{-4}$ in contrast to $\gamma_{geom} = (5.5 \pm 1.5) \times 10^{-2}$ calculated on the basis of the geometrical surface area of the sample and displayed in Table 3.

Table 3 Summary of uptake experiments with NO_3 on Kaolinite as a function of sample mass at $[NO_3] = (7.0 \pm 1.0) \times 10^{11}$ cm^{-3}, orifice diameter = 8 mm, $A_s = 19.6$ cm^2

Mass/g	γ_{ss}	Number of nominal layers[c]	Number of formal layers[d]
0.005[a]	$(5.0 \pm 2.0) \times 10^{-3}$	0.02	1
0.013[a]	$(1.0 \pm 0.5) \times 10^{-2}$	0.05	3
0.03[a]	$(1.1 \pm 0.6) \times 10^{-2}$	0.12	6
0.11[a]	$(2.9 \pm 1.1) \times 10^{-2}$	0.44	22
0.25[b]	$(3.0 \pm 1.1) \times 10^{-2}$	1	50
0.4[b]	$(4.8 \pm 1.5) \times 10^{-2}$	1.6	82
0.7[b]	$(5.5 \pm 1.5) \times 10^{-2}$	2.8	143
1[b]	$(5.5 \pm 1.6) \times 10^{-2}$	4	204

[a] Sprayed sample. [b] Powder sample. [c] Calculated for average grain size of 50 μm. [d] Calculated for average grain size of 1 μm disclosed by the manufacturer albeit without documentation.

In order to show that this underestimation of γ from the application of the KLM model or the BET surface is excessive we have performed NO_3 and NO_2 uptake experiments on activated molecular sieve particles that consist of macroscopic rods with a certified pore diameter of 3, 5 and 10 Å.

The strategy of this experiment is to compare γ_{ss} of NO_3 between a microporous material whose average pore diameter enables penetration of the NO_3 probe, and one that does not allow for pore diffusion because of geometrical constraints. In case no large increase of γ_{ss} is observed in going from small to large pore size one must conclude that pore diffusion will not occur to a significant extent during the lifetime of NO_3 in the reactor.

We chose the following molecular sieve particles having micropores of different diameters: $K_{12}[(AlO_2)]_{12}$ $(SiO_2)_{12}] \cdot XH_2O$, $Ca_{12}[(AlO_2)]_{12}(SiO_2) \cdot XH_2O$ and $Na_{86}[(AlO_2)_{86}(SiO_2)_{106}] \cdot XH_2O$ (Fluka) having pore diameters of 3, 5 and 10 Å, respectively, and where X represents the equilibrium H_2O content exclusive of water remaining adsorbed in the molecular pores. In order to rid the sample of adsorbed water the molecular sieves have been activated by pumping and heating to 200 °C. For 9 g of molecular sieve which resulted in the complete coverage of the 19.6 cm^2 sample support we estimated an external surface area of 1.6×10^2 cm^2 leading to 1.8×10^{-3} m^2 g^{-1}. The internal surface area for molecular sieves of different diameter has been reported in Table 4 and is consistent with a ratio r of internal to external surface area of 2.5×10^5, 1.95×10^5 and 1.4×10^5, respectively, for the molecular sieve materials listed in Table 4. We estimate that NO_3 has a characteristic size of approximately 4.5 Å which would lead to a surface density of approximately 5×10^{14} molecule cm^{-2} for one formal monolayer. Therefore, uptake of NO_3 on molecular sieve of 3 Å pore size should not take place on the internal surface of the pores in contrast to 5 and 10 Å molecular sieve where extensive pore diffusion of NO_3 is expected, given sufficient interaction time. As displayed in

Table 4 Summary of the uptake experiments of NO_3 and NO_2 on 9 g of activated molecular sieve particles of different pore size: steady state (γ_{ss}) uptake coefficients at an orifice diameter = 8 mm and $A_s = 19.6$ cm^2

Molecular sieve particles (nominal pore diameter/Å)	γ_{ss}, $[NO_3] = (7.0 \pm 1.0) \times 10^{11}$ cm^{-3}	γ_{ss}, $[NO_2] = (3.0 \pm 1.0) \times 10^{11}$ cm^{-3}	BET surface area/m^2 g^{-1},[44]	r[a]
10	$(1.0 \pm 0.3) \times 10^{-2}$	$(1.2 \pm 0.2) \times 10^{-3}$	455	2.5×10^5
5	$(7.8 \pm 3.1) \times 10^{-3}$	$(7.4 \pm 1.3) \times 10^{-4}$	333	1.9×10^5
3	$(5.7 \pm 2.2) \times 10^{-3}$	$(7.1 \pm 1.9) \times 10^{-4}$	243	1.4×10^5

[a] Ratio of internal to external surface area.

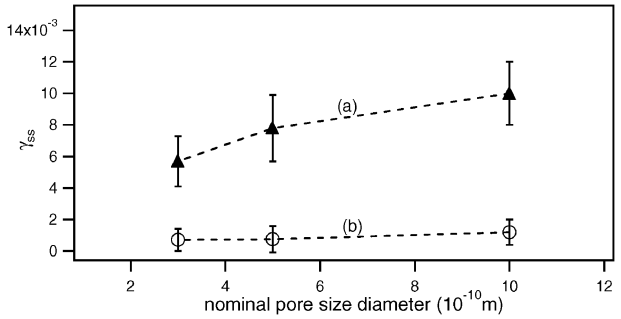

Fig. 4 Uptake experiment performed on activated molecular sieve samples: γ_{ss} as a function of the certified pore diameter. Triangles: $[NO_3] = (7.0 \pm 1.0) \times 10^{11}$ cm^{-3} ($k_{esc} = 1.75$ s^{-1}), Circles: $[NO_2] = (6.0 \pm 1.0) \times 10^{11}$ cm^{-3} ($k_{esc} = 2.0$ s^{-1}). All experiments have been performed at an orifice diameter of 8 mm and a surface sample area A_s of 19.6 cm^2.

Fig. 4 and reported in Table 4, γ_{ss} for the 3 and 5 Å pore size molecular sieve samples were found to be identical within experimental uncertainty. In addition, for molecular sieve particles of nominal 10 Å pore diameter we observed a γ_{ss} value larger by a factor 1.7 at a residence time of 0.58 s (8 mm orifice) for NO_3. The spread in γ_{ss} between the different molecular sieves is only a factor of 1.7, whereas we expected NO_3 to explore the internal microporous structure of the 5 and certainly of the 10 Å molecular alumosilicate sieve material, both of which are expected to lead to a marked increase in γ_{ss}. We emphasize that the three microporous materials had identical interstitial voids because ceramic particles of identical dimension have been used in experiments using the same mass for all three types of molecular sieve. Therefore the packing was identical for all experiments.

We conclude that on the time scale of our experiment NO_3 does not explore the internal surface of the pores where pore diffusion is expected on geometrical grounds, namely on the 5 and 10 Å molecular sieves. The same result has been obtained employing the less reactive radical NO_2 whose extent of pore diffusion is expected to be larger in view of its smaller γ value as displayed in Fig. 4.

We take this result as convincing justification to use the geometric surface area in evaluating the gas–surface collision frequency ω (eqn (E.5)) under the constraint of the present experimental condition of low gas-phase residence times. We think that the present conclusion may overestimate the true γ value by up to a factor of two if we approximate the shape of the ceramic material by a half sphere and assume a closely-packed arrangement. According to Table 5 we use Kaolinite as a typical example to extrapolate the kinetics to the other samples because its γ_0 is smallest compared to the other examined substrates. However, we also note that γ_0 is almost identical for all investigated samples within experimental uncertainty (Table 5).

Table 5 reports all results concerning experiments performed on 1–2 g of surrogate mineral dust powder at the high concentration of $[NO_3] = (4.0 \pm 1.0) \times 10^{12}$ cm^{-3}. The steady-state uptake coefficients γ_{ss} of NO_3 range from $(1.4 \pm 0.4) \times 10^{-2}$ for $CaCO_3$ to $(6.5 \pm 1.1) \times 10^{-2}$ for Saharan Dust using the geometric surface area. At the lower concentration of $[NO_3] = (7.0 \pm 1.0) \times 10^{11}$ cm^{-3} we found larger γ values ranging from $(3.4 \pm 1.6) \times 10^{-2}$ for natural limestone to (0.12 ± 0.08) for Saharan Dust compared to the experiments at higher $[NO_3]$.

The results for $[NO_3] = (7.0 \pm 1.0) \times 10^{11}$ cm^{-3} at a small sample mass ranging between 5 and 25 mg (sprayed samples) lead to an initial uptake coefficient γ_0 ranging from $(4.2 \pm 1.6) \times 10^{-3}$ for natural limestone to $(1.7 \pm 0.4) \times 10^{-2}$ for Saharan Dust. The lower values of γ_0 are certainly due to the fact that the low sample mass does not afford a coherent surface coating of the sample holder.

In Table 5 we also report the measured γ_0 values for NO_3 on all the samples of mineral dust at low and high values of $[NO_3]$. For the low value of $[NO_3] = (7.0 \pm 1.0) \times 10^{11}$ cm^{-3} the γ values range from 0.12 ± 0.08 for Kaolinite to 0.23 ± 0.2 for Saharan Dust. At the high value of $[NO_3] = (4.0 \pm 1.0) \times 10^{12}$ cm^{-3} the values range from 0.12 ± 0.04 for Kaolinite to 0.2 ± 0.07 for natural limestone. In comparison, γ_{ss} is lower only by a factor of two relative to γ_0 obtained at the same experimental conditions of low $[NO_3]$. Table 5 reveals in general that the values of γ_{ss} and γ_0 are larger for low compared to high values of $[NO_3]$ which we attribute to partial saturation of adsorption sites for NO_3. We take the small difference between γ_0 and γ_{ss} at both values of $[NO_3]$ as an additional confirmation for the absence of pore diffusion because γ_0 should only be minimally affected by pore diffusion and is expected to come close to the true value of the initial uptake coefficient. As already pointed out above, γ_0 is similar for all samples. However, this is not the case for γ_{ss} which reflects the different saturation behavior of the mineral dust samples which is also the reason for the increasing difference between γ_0 and γ_{ss} with increasing $[NO_3]$.

Several uptake experiments of NO_3 on 1 g of Kaolinite powder were carried out at different $[NO_3]$ (Table 6). Fig. 5 displays data for the 8 and 4 mm escape orifice corresponding to a residence time τ_g of 0.57 s and 2.1 s, respectively, for a variation of $[NO_3]$ between 5.5×10^{11} and 9.3×10^{12} cm^{-3}. We observe two limiting values of γ_{ss}: a) for $[NO_3]$ increasing from 5.5×10^{11} cm^{-3} to 1.8×10^{12} cm^{-3} γ_{ss} decreases from $(1.7 \pm 0.4) \times 10^{-1}$ to $(3.5 \pm 1.1) \times 10^{-2}$, b) for $[NO_3]$ between 1.8×10^{12} cm^{-3} and 9.3×10^{12} cm^{-3} γ_{ss} is constant at $(3.2 \pm 1.4) \times$

Table 5 Summary of uptake experiments of NO_3 on mineral dust samples at limiting masses: initial (γ_0) and steady state (γ_{ss}) uptake coefficients at an orifice diameter = 8 mm, $A_s = 19.6$ cm^2

Mineral dust sample	Mass/g	γ_{ss} $[NO_3]_0 = (7.0 \pm 1.0)$ x 10^{11} cm^{-3}	γ_{ss} $[NO_3]_0 = (4.0 \pm 1.0) \times 10^{12}$ cm^{-3}
$CaCO_3$	2	$(6.7 \pm 4.0) \times 10^{-2}$	$(1.4 \pm 0.4) \times 10^{-2}$
Natural limestone	2	$(3.4 \pm 1.6) \times 10^{-2}$	$(2.2 \pm 0.5) \times 10^{-2}$
Kaolinite	1	0.14 ± 0.02	$(5.0 \pm 1.4) \times 10^{-2}$
Saharan Dust	1	0.12 ± 0.08	$(6.5 \pm 1.2) \times 10^{-2}$
Arizona Test Dust	2	0.1 ± 0.06	$(2.5 \pm 0.7) \times 10^{-2}$
	Mass/g	γ_0 $[NO_3]_0 = (7.0 \pm 1.0) \times 10^{11}$ cm^{-3}	γ_0 $[NO_3]_0 = (4.0 \pm 1.0) \times 10^{12}$ cm^{-3}
$CaCO_3$	2	0.13 ± 0.1	0.14 ± 0.05
Natural limestone	2	0.12 ± 0.08	0.20 ± 0.07
Kaolinite	1	0.11 ± 0.08	0.12 ± 0.04
Saharan Dust	1	0.23 ± 0.2	0.16 ± 0.05
Arizona Test Dust	2	0.2 ± 0.1	0.14 ± 0.04

10^{-2} within experimental uncertainty and independent of $[NO_3]$. From this series of measurements it is evident that γ_{ss} follows a rate law pseudo first order in NO_3 at $[NO_3] > 1.8 \times 10^{12}$ cm^{-3}. Conversely, at $[NO_3] < 1.8 \times 10^{12}$ cm^{-3} the inverse dependence of γ_{ss} on $[NO_3]$ suggests that the mechanism of NO_3 uptake is complex and does not correspond to simple first-order uptake.

A similar dependence has been observed before by Hanisch and Crowley[28] in their work on ozone decomposition on Saharan dust and by Sullivan and coworkers[40] in their study of ozone decomposition on fresh alumina films. The reason for this behaviour may be related to the finite number of available surface sites of the substrate that are not completely saturated at low $[NO_3]$ resulting therefore in a larger uptake coefficient compared to high $[NO_3]$. It is the interplay between the finite number of adsorption sites and the competitive rates of desorption and surface reaction of NO_3 that leads to this typical inhibition behaviour that was also observed for other free radicals interacting with a solid substrate, so for example for NO_2 interacting with soot.[41]

Further experiments performed on natural limestone and $CaCO_3$ showed a strong dependence of γ_{ss} on the gas residence time at $[NO_3] = 2.3 \times 10^{12}$ cm^{-3} suggesting that the mechanism of NO_3 uptake is complex and does not correspond to a simple first order uptake reaction as already pointed out for Kaolinite. The γ_{ss} value decreased from $(5.1 \pm 2.0) \times 10^{-2}$ to $(2.7 \pm 1.1) \times 10^{-2}$ in going from $\tau_g = (1/k_{esc}) = 0.24$ s ($k_{esc} = 4.15$ s^{-1}) to $\tau_g = 1.85$ s ($k_{esc} = 0.54$ s^{-1}). These observations indicate that the reactivity of NO_3 on natural limestone and $CaCO_3$ decreases for long gas residence times τ_g as the heterogeneous reaction rate not only depends on the gas phase concentration but apparently also on intermediates whose surface concentration depend on the extent of reaction that scales with τ_g.

4. Reaction products

In all experiments adsorbed NO_3 gave rise to uptake of NO_2 that is associated with the NO_3 source. It is important to note that NO_2 itself did not show any uptake on the mineral dust surrogates, except for Saharan Dust, where $\gamma_{ss} = (3.1 \pm 0.5) \times 10^{-3}$ has been observed for pure NO_2 uptake. For 250 mg of Kaolinite we have observed the formation of small amounts of gas phase reaction products such as N_2O_5 and HNO_3. Using relation (E.8) we have calculated the rate of formation of N_2O_5 from the increase of the MS signal at m/z 46, I_{exc}^{46} displayed in Fig. 6 (curve (c)). The yield of N_2O_5 following the uptake of NO_3 decreased with increasing saturation of Kaolinite which may be explained by the slow deactivation of reactive surface sites and by the complete saturation of the NO_3 uptake at the end of the exposure time after the adsorption of 9.5×10^{17} NO_3 molecules (Fig. 6 (curve b)). In the NO_3 uptake on 250 mg of Kaolinite we also observed a small contribution to m/z 63,

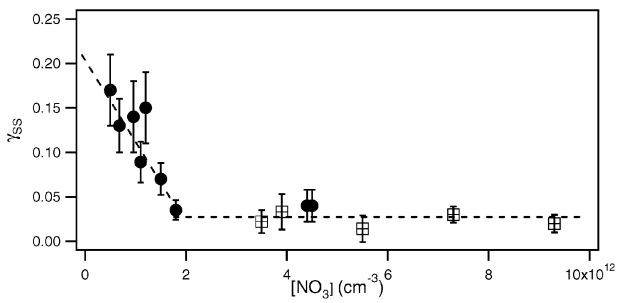

Fig. 5 NO_3 on Kaolinite: uptake coefficient γ_{ss} of NO_3 as a function of $[NO_3]$ ($A_s = 19.6$ cm^2). Full circles and squares represent the experimental uptake values obtained at 4 and 8 mm orifice diameter, respectively.

Table 6 Uptake experiments of NO_3 on 1 g of Kaolinite: steady state (γ_{ss}) uptake coefficients ($A_s = 19.6$ cm)

$[NO_3]$ cm^{-3}	γ_{ss}
[a] 5.0×10^{11}	$(1.7 \pm 0.4) \times 10^{-1}$
[a] 6.8×10^{11}	$(1.3 \pm 0.3) \times 10^{-1}$
[a] 9.6×10^{11}	$(1.4 \pm 0.4) \times 10^{-1}$
[a] 1.1×10^{12}	$(8.9 \pm 2.3) \times 10^{-2}$
[a] 1.2×10^{12}	$(1.5 \pm 0.4) \times 10^{-1}$
[a] 1.5×10^{12}	$(7.0 \pm 1.8) \times 10^{-2}$
[a] 1.8×10^{12}	$(3.5 \pm 1.1) \times 10^{-2}$
[b] 3.5×10^{12}	$(2.2 \pm 1.3) \times 10^{-2}$
[b] 3.9×10^{12}	$(3.3 \pm 2.0) \times 10^{-2}$
[a] 4.4×10^{12}	$(5.0 \pm 1.6) \times 10^{-2}$
[a] 4.5×10^{12}	$(5.0 \pm 1.6) \times 10^{-2}$
[b] 5.5×10^{12}	$(1.4 \pm 1.5) \times 10^{-2}$
[b] 7.3×10^{12}	$(3.0 \pm 0.9) \times 10^{-3}$
[b] 9.3×10^{12}	$(2.0 \pm 1.0) \times 10^{-2}$

Experiments performed using an escape orifice diameter of: [a] 8 mm. [b] 4 mm.

$I_r^{63(HNO3)}$, related to the production of gas phase HNO_3 as displayed in Fig. 6 (curve (d)).

As pointed out above, NO_3 may be represented by a 4.5 Å diameter sphere with a projected surface area of 1.59×10^{-15} cm^2 molecule^{-1} which leads to a full surface coverage of 6.3×10^{14} molecules cm^{-2} per formal monolayer. The 250 mg sample has a total surface area of 5.5×10^4 cm^2 based on a BET surface area of 22 m^2 g^{-1} for Kaolinite. This leads to 1.3×10^{16} and 3.5×10^{19} NO_3 forming a monolayer on 250 mg Kaolinite based on the geometric and BET surface area, respectively. The total number of NO_3 given above would have been consumed on $9.5 \times 10^{17}/3.5 \times 10^{19} = 2.7\%$ of reactive sites based on the BET surface area. Another way of looking at the same data is to state that a turnover of approximately 80 NO_3 radicals on the geometric surface is necessary in order to deactivate a surface site for NO_3 reaction up to complete saturation (Fig. 6b).

Next to Kaolinite, samples of 250 mg of $CaCO_3$ have been the only samples to show formation of N_2O_5 and HNO_3 upon uptake of NO_3 (see Table 7). When the samples begin to saturate, the observed amounts of N_2O_5 and HNO_3 both decrease. In order to understand the reason for the gas phase production of N_2O_5 and HNO_3 we have to remind the reader that all the investigated samples have a non negligible amount of adsorbed water available on the substrate surface. The

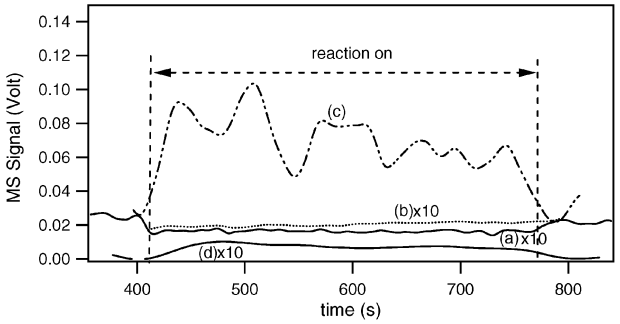

Fig. 6 Uptake of NO_3 on 250 mg of Kaolinite and resulting reaction products at $[NO_3] = (6.5 \pm 1.0) \times 10^{11}$ cm^{-3}. Curve (a) represents the raw MS signal at m/z 62 for the NO_3 uptake on the DELRIN® sample holder with Kaolinite, the dashed line (curve (b)) indicates $I_r^{62(NO3)}$ of the NO_3 uptake corrected for the DELRIN® contribution. Curve (c) is the calculated MS at m/z 46, I_{exc}^{46}, corresponding to N_2O_5 formation. The variable amplitude of curve (c) is a consequence of the large experimental uncertainty. Curve (d) represents the raw MS signal at m/z 63, $I_r^{63(NO3)}$, related to the production of gas phase HNO_3 (orifice diameter = 8 mm, $A_s = 4.9$ cm^2).

Table 7 Summary of reaction products during the heterogeneous reaction of NO_3 on 250 mg and 1 g of mineral dust surrogate samples at an orifice diameter of 8 mm

		Reaction products (250 mg)			Reaction products (1 g)		Adsorbed water	
Mineral dust sample	[a]γ_0	[c]N_2O_5	[c]HNO_3	[b]γ_{ss}	[d]N_2O_5	[d]HNO_3	$H_2O_{(ads)}$/mg g^{-1}	BET surface area/m^2 g^{-1}
$CaCO_3$	$(7.9 \pm 2.0) \times 10^{-2}$	12%	15%	$(1.4 \pm 0.8) \times 10^{-2}$	—	17%	4	5.06
Kaolinite	$(2.1 \pm 0.5) \times 10^{-2}$	23%	16%	$(5.0 \pm 1.5) \times 10^{-2}$	—	15%	23	22.57
Arizona Test Dust		—	—	$(2.5 \pm 1.0) \times 10^{-2}$	—	20%	22	
Saharan Dust		—	—	$(6.5 \pm 2.0) \times 10^{-2}$	—	—	20	39.6
Natural Limestone		—	—	$(1.2 \pm 0.4) \times 10^{-2}$	—	35%	7	

[a] Uptake experiment performed at $[NO_3]_0 = (7.0 \pm 1.0) \times 10^{11}$ cm^{-3}. [b] Uptake experiment performed at $[NO_3]_0 = (2.3 \pm 1.0) \times 10^{12}$ cm^{-3}. [c] Saturated sample (250 mg, $A_s = 4.9$ cm^2). [d] Non-saturated sample (1 g, $A_s = 19.6$ cm^2). The yield of N_2O_5 and HNO_3 is given as a percentage with respect to the total number of molecules of NO_3 taken up during the same reaction time. Dash (—) indicates a negative result for the experiment.

significant quantity of adsorbed $H_2O_{(ads)}$ that still remains on the different mineral dust substrates at our experimental conditions is reported in Table 7 and was measured by gravimetric measurements. Adsorbed water may therefore play an important role for the uptake of NO_3 on all samples examined in the Knudsen reactor.

Under our experimental conditions the formation of N_2O_5 may be related to the presence of NO_2 effusing from the NO_3 source *via* its reaction with adsorbed NO_3 on the mineral dust substrate. The observed simultaneous uptake for both NO_3 and NO_2 suggests the formation of $N_2O_{5(ads)}$ through the heterogeneous recombination reaction (5.a):

$$NO_{3(ads)} + NO_2 \rightarrow N_2O_{5(ads)} \quad (5.a)$$

The conversion of NO_3 to N_2O_5 occurs *via* an Eley–Rideal mechanism where NO_3 first adsorbs onto the dust surface as $NO_{3(ads)}$ and subsequently reacts with gas phase NO_2. This reaction is the interfacial analog of the well known gas-phase equilibrium:

$$NO_2 + NO_3 + M \leftrightarrows N_2O_5 + M \quad (5.b)$$

whose equilibrium constant is known from recent work.[42]

Once N_2O_5 has been adsorbed, it may desorb into the gas phase:

$$N_2O_{5(ads)} \rightarrow N_2O_{5(g)} \quad (5.c)$$

On the other hand, $N_2O_{5(ads)}$ may react with adsorbed water $H_2O_{(ads)}$ and form gas phase HNO_3, part of which may desorb into the gas phase, according to reaction (5.d):

$$N_2O_{5(ads)} + H_2O_{(ads)} \rightarrow 2HNO_{3(g)} \quad (5.d)$$

Additional NO_3 uptake experiments have been performed on all mineral dust samples at $[NO_3] = 2.3 \times 10^{12}$ cm^{-3} on 1.0 g of powder (see Table 7). Under these conditions we did not succeed in saturating the substrates at practical reaction times as they are apparently able to adsorb large amounts of NO_3. NO_3 uptake gave rise to gas phase HNO_3 formation for $CaCO_3$, Kaolinite, Arizona Test Dust and natural limestone without any visible trace of desorbing N_2O_5 from the surface. Fig. 7 displays raw data of an uptake experiment of NO_3 on 2 g of natural limestone showing the production of gas phase HNO_3 at a yield of 35% with respect to NO_3 taken up on the substrate. Of note is the fact that a small impurity of 0.5% and 0.3% of Al_2O_3 and Fe_2O_3, respectively, in natural limestone of 97% (by weight) $CaCO_3$ has a significant effect on the heterogeneous reaction of NO_3 as displayed in Table 7. The fact that we did not observe gas phase formation of N_2O_5 upon uptake of NO_3 on samples of 1 g, where large quantities of adsorbed water are present as displayed in Table 7, suggests that reaction (5.d) may be faster than reaction (5.c).

In order to probe for the presence of an adsorbed reactive species on the substrate during NO_3 uptake, experiments using NO and NO_2 were performed on all the examined substrates immediately after the uptake of known quantities of NO_3. The goal has been to determine whether or not the adsorbed NO_3 is able to react with NO or NO_2. On 1 g of Arizona Test Dust, uptake of NO on adsorbed NO_3 produced a small amount of NO_2 which has been observed using REMPI at $\lambda_{NO_2} = 511$ nm. On the time scale of this experiment of approximately 300 s, 1.3×10^{18} molecules of NO_3 have been adsorbed on the substrate. The reaction during 230 s with an excess of NO in the absence of gas phase NO_3 during 230 s resulted in a production of 3.2×10^{17} molecules of NO_2 which corresponds to a 12.3% retrieval of adsorbed NO_3.

On Saharan Dust that has previously been exposed to NO_3 and NO_2 we have observed uptake of NO but no visible trace of gas phase NO_2. As discussed above, NO_2 shows an uptake on virgin Saharan Dust samples. On exposed $CaCO_3$ and natural limestone samples, no NO uptake has been observed.

An additional experiment was carried out on 1 g of Saharan Dust where NO_2 was used as a probe for adsorbed NO_3. On 1 g of Saharan Dust, uptake of NO_2 on adsorbed NO_3 produced a small amount of excess NO_2 which has been observed using REMPI at $\lambda_{NO_2} = 511$ nm. On the time scale of this experiment of approximately 400 s, 8×10^{17} molecules of NO_3 have been adsorbed on 1 g of Saharan Dust. The reaction with an excess of NO_2 in the absence of gas phase NO_3 during 100 s resulted in a production of 1.8×10^{17} molecules of NO_2. The observed NO_2 production corresponds to 22.5% of adsorbed NO_3. In this case we did not observe any NO production using REMPI detection at $\lambda_{NO} = 452.6$ nm which is probably related to the

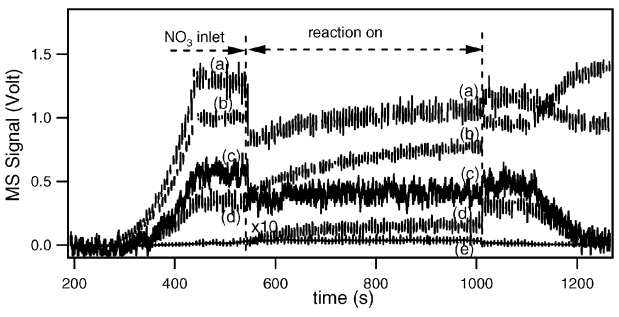

Fig. 7 NO_3 uptake on a sample of 2 g of natural limestone at $[NO_3] = (7.0 \pm 1.0) \times 10^{11}$ cm^{-3}. Curves (a), (b), (d) and (e) correspond to the raw MS signals monitored at m/z 30, 46, 62 and 63, respectively. Curve (c) corresponds to the raw REMPI signal for NO_2 detection at $\lambda_{NO_2} = 511$ nm converted to a MS signal at m/z 46 (orifice diameter = 8 mm, $A_s = 19.6$ cm^2).

fact that NO, if formed, may rapidly react with adsorbed NO_3 as discussed above.

For all the mineral dust substrates studied, the uptake of NO_3 on mineral dust was irreversible, at least on timescales used in this work. This was checked in experiments such as NO_3 uptake on Kaolinite where after approximately 7 minutes of exposure, the sample was isolated and the NO_3 flow subsequently turned off. When the isolation plunger was lifted again, no release of NO_3 was observed at m/z 62. Free radical adsorption on solid polar surfaces are known in the literature. For example, recent work has shown the adsorption of CH_3O_2 free radical on KCl surfaces and effective bimolecular reactions with NO_2 and organic molecules whose kinetic parameters revealed a heterogeneous mechanism.[43]

In summary, we must clearly point out that the uptake of NO_3 on mineral dust is not in any way catalytic in nature as exemplified in reactions (3) and (4). This conclusion is supported by the formation of volatile reaction products such as N_2O_5 and HNO_3 (Table 7) as well as by the complete eventual saturation of the NO_3 uptake on small mass samples of mineral dust as displayed in Fig. 6b. The chemical turnover or reaction rate of NO_3 is accompanied by the slow irreversible build-up of non-volatile reaction products leading to the final inhibition or saturation of NO_3 uptake.

5. Conclusions and atmospheric implications

We have shown in this work that NO_3 undergoes fast heterogeneous reactions with surrogate substrates of mineral dust aerosol at $T = 298 \pm 2$ K. Ancillary uptake experiments performed with NO_3 on molecular sieve alumosilicate particles of different nominal pore diameter have led to the conclusion that the pore diffusion correction is not appropriate for the present experimental conditions of relativity short contact times. Therefore, the geometric surface area of the dust sample has been used for the calculation of γ_0 and γ_{ss}. The measured uptake coefficient showed different values for high and low $[NO_3]$. At $[NO_3] = (4.0 \pm 1.0) \times 10^{12}$ cm^{-3} γ_{ss} ranged from $(1.4 \pm 0.4) \times 10^{-2}$ for $CaCO_3$ to $(6.5 \pm 1.1) \times 10^{-2}$ for Saharan Dust. At $[NO_3] = (7.0 \pm 1.0) \times 10^{11}$ cm^{-3} γ_{ss} ranged from $(3.4 \pm 1.6) \times 10^{-2}$ for natural limestone to (0.12 ± 0.08) for Saharan Dust.

These values are significantly larger than the ones used in a recent global modeling simulation of heterogeneous chemistry on mineral dust aerosol,[35] where a γ value of 3.0×10^{-3} for NO_3 has been used. However, the modeling study performed by Bian and Zender[34] used a γ value of 0.1 for NO_3. This value is in agreement with the one we obtained by extrapolation of γ to vanishing NO_3 concentration from our uptake experiments performed on Kaolinite as displayed in Fig. 5. We therefore have extrapolated the value of γ_{ss} for $[NO_3] < 5.0 \times 10^{11}$ cm^{-3}. With trophospheric $[NO_3]$ at a typical value of 2.0×10^9 cm^{-3}, γ_{ss} tends towards values larger than 0.2 ± 0.03 according to the results displayed in Fig. 5.

The present experimental results of γ for NO_3 seem to be more in agreement with the guess of Bian and Zender[34] compared to Bauer *et al.*[35] and suggests a significant removal of NO_3 in areas affected by mineral dust close to ground. This leads to a decrease of the oxidation potential of the atmosphere at night by virtue of the removal of NO_3 and the decrease of O_3 observed in all model results, albeit to a variable extent. However, the NO_3 removal also affects the abundance of HNO_3 because the nighttime sources are the heterogeneous hydrolysis of N_2O_5 and to a minor extent, the reaction of NO_3 with HO_2, both of which directly depend on NO_3.[35] It is therefore of some importance to obtain reliable values for the kinetics of key free radicals that control in part important precursors such as HNO_3 and N_2O_5.

The specific comparison of the results of Bauer *et al.*[35] and Bian and Zender[34] highlights the importance of key free radicals such as NO_3. The latter attribute a large reactivity to NO_3 and a small one to HNO_3, and *vice versa* for the former. However, the resulting trend in both models is the same, namely the decrease of O_3 through the reactive process of the ozone precursor NO_3 or HNO_3. The conclusion is that the resulting effect on the trace gas composition is insensitive to the detailed allocation of heterogeneous reactivity, provided the species in question are chemically coupled as for NO_3 and HNO_3.

In summary, this work delivers several messages of potential importance to atmospheric chemistry: (a) The uptake coefficient of NO_3 on mineral dust aerosol under tropospheric conditions is larger than 0.1 for a selection of surrogate mineral dust materials and does not seem to be affected by the presence of NO_2; (b) in contrast to the uptake kinetics the observed reaction products HNO_3 and N_2O_5 seem to depend on the presence of NO_2 and on the quantity of the available adsorbed H_2O; (c) a significant part of NO_3 that is disappearing from the gas phase seems to retain its reactivity in the adsorbed state as shown in experiments with NO_2 and NO; (d) the uptake of NO_3 on mineral dust is non-catalytic. Despite the open nitrogen mass balance a significant fraction of adsorbed NO_3 is expected to be released as volatile HNO_3 and N_2O_5 on mineral dust aerosol which is in fact observed in laboratory experiments.

Water is expected to play an important role because of the hydrolysis of N_2O_5, even under the present experimental (dry) conditions. Despite our inability to perform experiments at elevated humidity using the Knudsen flow reactor, we believe that H_2O cannot substantially alter the uptake kinetics in agreement with Sullivan *et al.*[40] Our laboratory observations also indicate that the reactivity of NO_3 on mineral dust aerosols decreases for long gas residence times τ_g as the heterogeneous reaction rate not only depends on the gas phase concentration but also on intermediates whose concentration depend on the extent of reaction. Despite the presence of NO_2 this work indicates that interaction with mineral dust may be an important loss process for tropospheric NO_3 whose quantitative consequences will have to be assessed by modeling studies. Therefore, the uptake of NO_3 on mineral dust aerosols may have a much greater influence on the reduction of O_3 as compared to the estimated value of 0.4% of global ozone reduction[35] for $\gamma_{NO_3} = 3.0 \times 10^{-3}$.

The NO_3 loss rate constant (k_{het}) due to heterogeneous uptake onto aerosol is given by $k_{het} = \tau^{-1}(NO_3) = \gamma A \bar{c}/4$ where γ is the uptake coefficient of NO_3 and is a function of the mineral dust aerosol composition, A is the surface area density of the dust and $\bar{c}$ is the mean molecular speed of NO_3. Assuming a surface area density of $A = 1.5 \times 10^{-6}$ cm^2 cm^{-3} for a dust plume[23] and $\gamma = 0.2$ from our extrapolated value for NO_3 we evaluated a lifetime of 22 min for NO_3. This value has to be compared to the diurnal photolysis of NO_3. During the day, NO_3 has a very short lifetime (about 5 s) due to its strong absorption in the visible region (662 nm) and its rapid photodissociation, mainly to NO_2 according to $NO_3 + h\nu \rightarrow NO_2 + O(^3P)$. Since this photochemical gas-phase loss process takes place only during the day, NO_3 loss by reaction on dust is important only during the night. Heterogeneous nighttime removal of NO_3 by mineral dust and formation of gas-phase HNO_3 after reacting with gas-phase NO_2 could change the NO_x/NO_y ratio during the night and in the presence of dust plumes.

Appendix

Resonance enhanced multiphoton ionization (REMPI) detection of NO_2 and NO in the Knudsen flow reactor

As displayed in Fig. 8, a Pyrex cell has been added to the main body of the reactor in order to enable *in situ* REMPI detection. Inside this REMPI cell two electrodes were mounted, each on

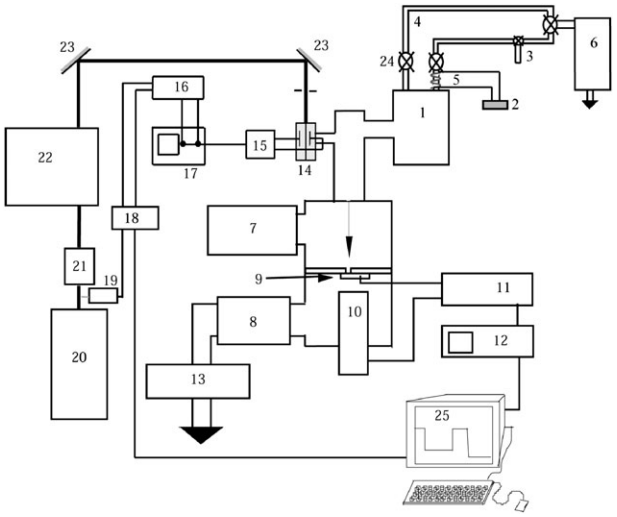

Fig. 8 Schematic drawing of the Knudsen cell reactor and view of the REMPI excitation and detection parts, including triggering and signal processing electronics. 1, Knudsen cell reactor; 2, variable potentiometer; 3, N_2O_5 sample; 4, gas inlet lines; 5, 6 cm hot glass tube of 0.6 cm diameter externally heated to 530 K using NiCr wire for the N_2O_5 inlet ($V = 1.7$ cm^3); 6, mechanical pump; 7, cryogenic pump; 8, turbo pump; 9, mechanical chopper; 10, quadrupole mass spectrometer; 11, lock-in amplifier; 12, oscilloscope; 13, dry pump; 14, pyrex cell for REMPI detection; 15, preamplifier; 16, boxcar integrator; 17, oscilloscope; 18, delayed beam triggering; 19, photodiode; 20, Nd:YAG laser; 21, dichroic harmonic separator; 22, PDL-3; 23, mirror; 24, inlet valve; 25, PC.

an electrical feedthrough. The electrodes consist of two polished Cu plates mounted in a cell that is equipped with two quartz windows for the entry and exit of a focused visible laser beam. The dye laser beam is focused by means of a 70 mm (focal length) plano-convex lens in the center of the two plate electrodes which are biased at ±65 V against ground. REMPI was performed using a Quanta Ray® PDL-3 dye laser pumped by the third harmonic of a Quanta Ray® Nd:YaG (GCR-3) laser at 355 nm which generates visible light in the wavelength range 420 to 520 nm. Two different dyes were used to study REMPI of NO and NO_2: Coumarin 120 (absorption $\lambda_{max} = 354$ nm[45]) and Coumarin 307 (absorption $\lambda_{max} = 395$ nm[45]) for NO and NO_2, respectively.

Ions and electrons created in the focal volume of the dye laser are collected by the plate electrodes, amplified and, after inversion of one of the signals, added before averaging by a box-car (SRS 250) integrator in order to yield the measured REMPI signal. The signal area A_{REMPI} resulting from the integration for 300 μs under the REMPI signal is proportional to the number of charge carriers initially generated by REMPI and so is directly proportional to the gas concentration $[M]_{REMPI}$ following eqn (E.A1):

$$[\mathrm{M}]_{\mathrm{REMPI}} = A_{\mathrm{REMPI}} C_{(\mathrm{M})\mathrm{REMPI}} \qquad \text{(E.A1)}$$

where $C_{(M)REMPI}$ is a calibration factor that is directly determined from an absolute determination of $[M]$ using a suitably calibrated MS signal for species M. In order to determine this calibration factor we monitored $[M]_{MS}$ against the integrated REMPI signal A_{REMPI} following eqn. (E.A2):

$$C_{(\mathrm{M})\mathrm{REMPI}} = \frac{[\mathrm{M}]_{\mathrm{MS}}}{A_{\mathrm{REMPI}}} \qquad \text{(E.A2)}$$

Previous studies have already examined the complexity of the REMPI spectrum of NO at ambient temperature. Nitric oxide can be ionized by four photons including both two and three-photon resonances. The two-photon resonances are found to be much more intense than the three-photon ones. Absorption of two more photon promotes the excited state molecule above its ionization potential and the molecule spontaneously ionizes.[46] The excitation process is depicted in Fig. 9 and corresponds to a [2 + 2] process: two photons at $\lambda_{NO} = 452.6$ nm resonantly excite NO in the $X^2\Pi \rightarrow A^2\Sigma^+$ band.[47,48] Two additional photons at $\lambda_{NO} = 452.6$ nm are absorbed between the $A^2\Sigma^+$ states and the vibrational Rydberg levels resulting in the ionization of the molecule. The overall process is described by the following reactions:

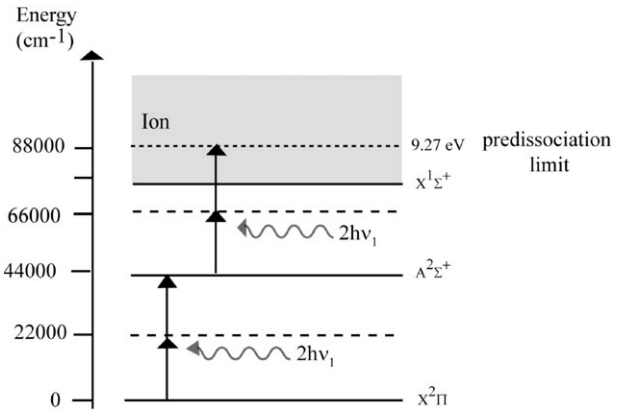

Fig. 9 Energy level diagram showing the two-photon resonant, four-photon ionization of nitric oxide *via* vibrations of the $A^2\Sigma^+$ state. The final four-photon energy in the continuum (shaded region) and the ionization energy (dashed line) are indicated.

$$\mathrm{NO}(\mathrm{X}^2\Pi) + 2h\nu_1 \rightarrow \mathrm{NO}(\mathrm{A}^2\Sigma^+) \qquad \text{(A1)}$$

$$\mathrm{NO}(\mathrm{A}^2\Sigma^+) + 2h\nu_1 \rightarrow \mathrm{NO}^+ + \mathrm{e}^- \qquad \text{(A2)}$$

The REMPI spectrum of NO and the energy of the dye laser (Coumarin 120) near 452 nm is shown in Fig. 10. The region of major intensity of the REMPI spectrum ranges between 451.2 and 452.4 nm, the most intense narrow peak is at $\lambda_{NO} = 452.6$ nm.

In order to ionize NO_2 we have used a one color excitation scheme requiring four photons. The nature of the process is revealed by a resonance involving a three-photon transition from the ground state to a vibrational level of a 3s Rydberg state originating near 50000 cm^{-1}.[48,49] The complete excitation process presented in the diagram displayed in Fig. 11 corresponds to a [3 + 1] mechanism: one photon at $\lambda_{NO_2} = 511$ nm NO_2 resonantly excites NO_2 in the band connecting the ground state X^2A_1 to a virtual intermediate state. At our chosen excitation wavelength of 511 nm, the two-photon energy for wavelengths longer than 498.2 nm falls just short of the origin of the 249.1 nm B^2B_2 state in NO_2. Both excited state levels, namely A^2B_2, A^2B_1 of NO_2 are not involved in the electronic transition at $\lambda_{NO_2} = 511$ nm. Therefore, it has to take place *via* a virtual intermediate level located above A^2B_1. Two additional photons at $\lambda_{NO_2} = 511$ nm are resonantly absorbed from

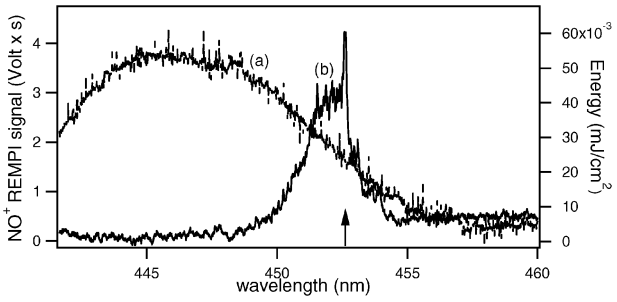

Fig. 10 REMPI spectrum of NO between 442 and 460 nm (trace (b)) compared with the corresponding gain curve of the laser dye (Coumarin 120, absorption $\lambda_{max} = 354$ nm[45] used for the ionization process (curve (a)). The sharp peak located at $\lambda_{NO} = 452.6$ nm has been used to monitor NO (arrow).

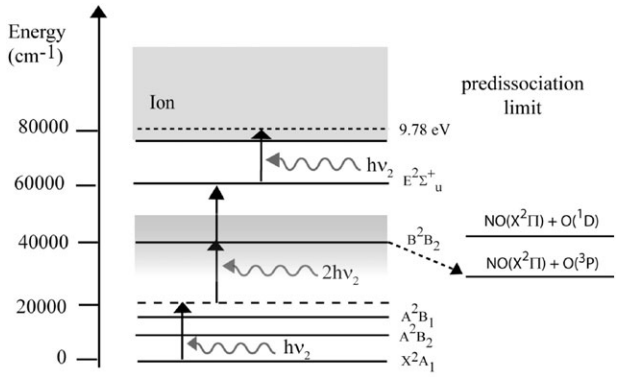

Fig. 11 Energy level diagram showing the three-photon resonant, four-photon ionization of NO_2 *via* vibrations of the B^2B_2 state. The NO_2 dissociation to yield neutral $NO(X^2\Pi)$ and $O(^3P)$ is indicated (dashed arrow). The final four-photon energy in the continuum (shaded region) and the ionization energy (dashed line) are indicated.

this virtual state to the four photon excited state *via* the $E^2\Sigma_u^+$ Rydberg levels.[50]

The complete excitation process may be viewed as a [3 + 1] ionization process, with the spectral structure reflecting the resonance at the three-photon level:

$$NO_2(X^2A_1) + 3h\nu_2 \rightarrow NO_2\,(E^2\Sigma_u^+) \qquad (A3)$$

$$NO_2(E^2\Sigma_u^+) + h\nu_2 \rightarrow NO_2{}^+ + e^- \qquad (A4)$$

The REMPI spectrum of NO_2 and the energy of the dye laser (Coumarin 307) near 511 nm is shown in Fig. 12. The high level background below the REMPI signal, visible at $\lambda = 511$ nm is due to vibrationally excited NO produced from NO_2 dissociation during the excitation/photoionization process. The resulting spectrum is thus the sum of an ionization spectrum for NO_2 overlaid on a continuous ionization spectrum for NO generated by photodissociation of NO_2.[50] In this case molecular NO_2 undergoes a transition to the electronically excited B^2B_2 dissociative state, producing vibrationally excited $NO(X^2\Pi)$ which then interacts with the laser beam as displayed in Fig. 13. The fact that we observe a REMPI signal presumably due to NO^+ above 500 nm shows that two-photon dissociation of NO_2 must occur below the origin of the B^2B_2 state. Energetically speaking, the only possible pathway is to $NO(X^2\Pi) + O(^3P)$, and as anticipated, the NO^+ spectrum is continuous and unassignable in this region.[50] An ancillary REMPI experiment has been performed by exciting a flow of pure NO at $\lambda_{NO_2} =$ 511 nm. As expected, we did not observe any NO^+ REMPI signal which must mean that NO was formed with significant excess energy during NO_2 excitation enabling REMPI detection of NO_2 at $\lambda_{NO_2} = 511$ nm.[50]

In order to examine the kinetics of the rate-limiting step of the REMPI process for NO_2 and NO we have studied the dependence of the $NO_2{}^+$ ion yield as a function of laser

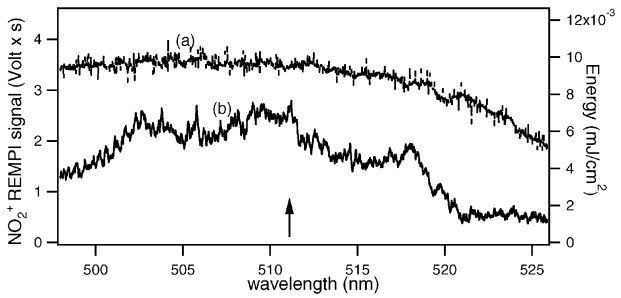

Fig. 12 REMPI spectrum of NO_2 between 500 and 525 nm (trace (b)) compared to the corresponding gain curve of the laser dye (Coumarin 307, absorption $\lambda_{max} = 395$ nm[45]) used for the ionization process (curve (a)). $\lambda_{NO_2} = 511$ nm was used for detection of NO_2 (arrow).

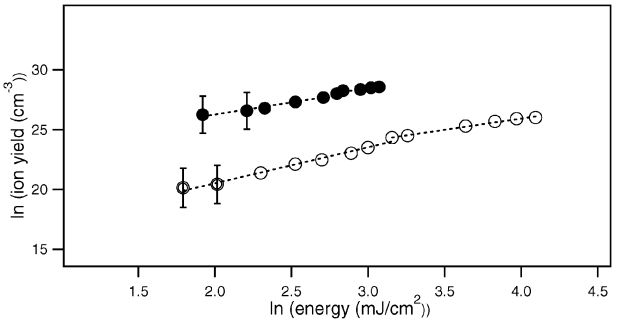

Fig. 13 REMPI signal for NO and NO_2 excitation at 452.6 nm and 511 nm, respectively. The filled and open circles represent experimental data for NO and NO_2, respectively. The fit of the data to a power law is shown as the dashed lines.

intensity. At the limit of low intensities or small cross sections, that is in the absence of significant saturation, the overall ionization is simply given by the following expression of absorption:[51]

$$N = \sigma_I\sigma_{II}I^{n+m} \qquad (E.A3)$$

In this eqn. (1) represents the laser intensity, $\sigma_I I^n$ the transition probability for the n-resonant transitions and $\sigma_{II}I^m$ the transition probability for the m ionization photons. σ_I and σ_{II} are the cross-sections for the n-photon transition and m-photon-ionization, respectively. Typical values for NO cross-sections are: σ_I (two photon; NO) $= 4.8 \times 10^{-51}$ cm^4 s and σ_{II} (two-photon; NO) $= 2.0 \times 10^{-49}$ cm^4 s, obtained from the theoretical calculation of the two-photon resonant excitation of NO and of the two-photon ionization of NO.[52] For NO_2, typical values for NO_2 cross-sections are: σ_I (three-photon; NO_2) $= 2.6 \times 10^{-82}$ cm^6 s^2 and σ_{II} (one-photon; NO_2) $= 2.0 \times 10^{-20}$ cm^2, obtained for the theoretical calculation of the three-photon resonant excitation of NO_2 and the one-photon ionization of NO_2.[52]

At moderate laser intensities, the ionization rate is saturated and the overall ionization probability is proportional to:

$$N = \sigma_I I^n \qquad (E.A4)$$

As displayed in Fig. 13 the measurement of the yield of NO^+ ($\lambda_{NO} = 452.6$ nm) *versus* laser intensity showed an I^2 and $I^{1.7}$ dependence at low and high laser intensities, respectively, whereas $NO_2{}^+$ ($\lambda_{NO_2} = 511$ nm) showed an $I^{2.9}$ and $I^{1.9}$ dependence at low and high laser intensities, respectively. Therefore, the NO^+ and $NO_2{}^+$ REMPI spectra are controlled by the $X^2\Pi \xrightarrow{2h\nu} A^2\Sigma^+$ and $X^2A_1 \xrightarrow{3h\nu} E^2\Sigma_u^+$ transitions, respectively.

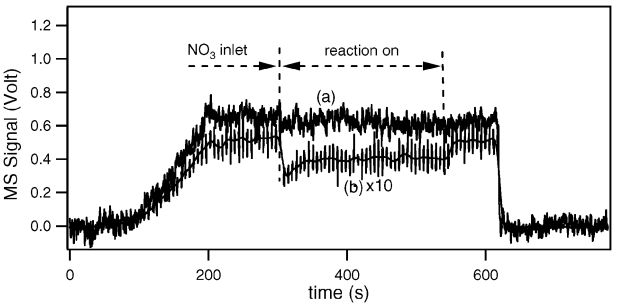

Fig. 14 Simultaneous measurement of the NO_3 uptake on a DELRIN sample holder using MS at m/z 62 (curve (b)) and the REMPI signal for NO_2 at $\lambda_{NO_2} = 511$ nm converted to a MS signal at m/z 46 (curve (a)). $[NO_3] = (7.0 \pm 1.0) \times 10^{11}$ cm^{-3} at orifice diameter 8 mm. The constant REMPI NO_2 signal that is equivalent to the displayed MS signal in the presence of the changing NO_3 MS signal, upon NO_3 uptake, indicates that NO_3 secondary photolysis at $\lambda_{NO_2} = 511$ nm does not contribute to the NO_2 REMPI signal according to $NO_3 + h\nu \rightarrow NO_2 + O(^3P)$.

The conditions chosen for REMPI detection of NO_2 and NO did not show a measurable contribution from the photodissociation of NO_3 which otherwise would have complicated the interpretation of the present results owing to secondary photolysis at $\lambda_{NO_2} = 511$ nm and $\lambda_{NO} = 452.6$ nm. Fig. 14 displays an auxiliary experiment of NO_3 interacting with the DELRIN® support that has been carried out in order to show that the uptake of NO_3 on DELRIN® ($\gamma_{DELRIN} = 8.2 \times 10^{-3}$) and the subsequent decrease of the m/z 62 (NO_3^+) does not affect the REMPI signal for NO_2 present as an impurity from the NO_3 source. Moreover, NO_2 did not show any uptake on DELRIN® under all conditions.

On the other hand, REMPI detection of NO at $\lambda_{NO} = 452.6$ nm leads to some two-photon photodissociation of NO_2, if present. In order to prove the photodissociation of NO_2 and subsequent ionization of the product NO under NO REMPI detection conditions, we photoionized a flow of pure NO at $\lambda_{NO} = 452.6$ nm. Subsequently, we introduced an additional flow of pure NO_2 identical to [NO] and observed an increase in the NO REMPI signal of approximately (20 ± 5)% of that of the original NO (at 20 mJ cm^{-2} power). This means that the REMPI detection of NO at $\lambda_{NO} = 452.6$ nm will lead to an additional REMPI signal if NO_2 is present at the same time as NO.

Acknowledgements

We gratefully acknowledge the Office Fédéral de l'Enseignement et de la Science (OFES) for funding this work in the context of the Fifth Framework Program of the EU, subproject MINATROC which is part of the EU Environment and Climate Program.

References

1 R. P. Wayne, I. Barnes, P. Biggs, J. P. Burrows, C. E. Canosamas, J. Hjorth, G. Lebras, G. K. Moortgat, D. Perner, G. Poulet, G. Restelli and H. Sidebottom, *Atmos. Environ. A*, 1991, **25**, 1–203.
2 U. Platt, G. Lebras, G. Poulet, J. P. Burrows and G. Moortgat, *Nature*, 1990, **348**, 147–149.
3 D. Mihelcic, D. Klemp, P. Musgen, H. W. Patz and A. Volz-Thomas, *J. Atmos. Chem.*, 1993, **16**, 313–335.
4 J. P. Naudet, P. Rigaud and M. Pirre, *J. Geophys. Res. Atmos.*, 1989, **94**, 6374–6382, DOI: 10.1029/88JD03856.
5 U. Platt, D. Perner, G. W. Harris, A. M. Winer and J. N. Pitts, *Nature*, 1980, **285**, 312–314.
6 K. Thomas, A. Volz-Thomas, D. Mihelcic, H. G. J. Smit and D. Kley, *J. Atmos. Chem.*, 1998, **29**, 17–43.
7 F. Gratpanche and J. P. Sawerysyn, *J. Chim. Phys.-Chim. Biol.*, 1999, **96**, 213–231.
8 M. Y. Gershenzon, S. Il'in, N. G. Fedotov, Y. M. Gershenzon, E. V. Aparina and V. V. Zelenov, *J. Atmos. Chem.*, 1999, **34**, 119–135.
9 Y. Rudich, R. K. Talukdar and A. R. Ravishankara, *J. Geophys. Res.-Atmos.*, 1998, **103**, 16133–16143, DOI: 10.1029/98JD01280.
10 S. Seisel, F. Caloz, F. F. Fenter, H. van den Bergh and M. J. Rossi, *Geophys. Res. Lett.*, 1997, **24**, 2757–2760, DOI: 10.1029/97GL02857.
11 A. R. Ravishankara, *Science*, 1997, **276**, 1058–1065.
12 D. J. Jacob, *Atmos. Environ.*, 2000, **34**, 2131–2159.
13 R. R. Dickerson, S. Kondragunta, G. Stenchikov, K. L. Civerolo, B. G. Doddridge and B. N. Holben, *Science*, 1997, **278**, 827–830.
14 S. He and G. R. Carmichael, *J. Geophys. Res.-Atmos.*, 1999, **104**, 26307–26324, DOI: 10.1029/1999JD900789.
15 R. V. Martin, D. J. Jacob, R. M. Yantosca, M. Chin and P. Ginoux, *J. Geophys. Res.-Atmos.*, 2003, **108**, art. no. 4097, DOI: 10.1029/2002JD002622.
16 H. Liao, P. J. Adams, S. H. Chung, J. H. Seinfeld, L. J. Mickley and D. J. Jacob, *J. Geophys. Res.-Atmos.*, 2003, **108**, art. no. 4001, DOI: 10.1029/2001JD001260.
17 I. Tegen and R. Miller, *J. Geophys. Res.-Atmos.*, 1998, **103**, 25975–25995, DOI: 10.1029/98JD02345.
18 I. Tegen and I. Fung, *J. Geophys. Res.-Atmos.*, 1994, **99**, 22897–22914, DOI: 10.1029/94JD01928.
19 S. Engelstaedter, K. E. Kohfeld, I. Tegen and S. P. Harrison, *Geophys. Res. Lett.*, 2003, **30**, 1294, DOI: 10.1029/2002GL016471.
20 J. M. Prospero, *Proc. Natl. Acad. Sci. USA*, 1999, **96**, 3396–3403.
21 L. Gomes and D. A. Gillette, *Atmos. Environ. A*, 1993, **27**, 2539–2544.
22 Y. Zhang, Y. Sunwoo, V. Kotamarthi and R. Carmichael, *J. Appl. Meteorol.*, 1994, **33**, 813–824.
23 M. de Reus, F. Dentener, A. Thomas, S. Borrmann, J. Strom and J. Lelieveld, *J. Geophys. Res. Atmos.*, 2000, **105**, 15263–15275.
24 P. Bonasoni, P. Cristofanelli, F. Calzolari, U. Bonafe, F. Evangelisti, A. Stohl, S. Z. Sajani, R. van Dingenen, T. Colombo and Y. Balkanski, *Atmos. Chem. Phys.*, 2004, **4**, 1201–1215.
25 C. R. Usher, A. E. Michel and V. H. Grassian, *Chem. Rev.*, 2003, **103**, 4883–4939.
26 F. Hanisch and J. N. Crowley, *Phys. Chem. Chem. Phys.*, 2001, **3**, 2474–2482.
27 F. Hanisch and J. N. Crowley, *J. Phys. Chem. A*, 2001, **105**, 3096–3106.
28 F. Hanisch and J. N. Crowley, *Atmos. Chem. Phys.*, 2003, **3**, 119–130.
29 F. Hanisch and J. N. Crowley, *Phys. Chem. Chem. Phys.*, 2003, **5**, 883–887.
30 N. Carslaw, J. M. C. Plane, H. Coe and E. Cuevas, *J. Geophys. Res. Atmos.*, 1997, **102**, 10613–10622.
31 M. Vrekoussis, M. Kanakidou, N. Mihalopoulos, P. J. Crutzen, J. Lelieveld, D. Perner, H. Berresheim and E. Baboukas, *Atmos. Chem. Phys.*, 2004, **4**, 169–182.
32 F. J. Dentener, G. R. Carmichael, Y. Zhang, J. Lelieveld and P. J. Crutzen, *J. Geophys. Res. Atmos.*, 1996, **101**, 22869–22889, DOI: 10.1029/96JD01818.
33 A. Tabazadeh, M. Z. Jacobson, H. B. Singh, O. B. Toon, J. S. Lin, R. B. Chatfield, A. N. Thakur, R. W. Talbot and J. E. Dibb, *Geophys. Res. Lett.*, 1998, **25**, 4185–4188, DOI: 10.1029/1998GL900062.
34 H. S. Bian and C. S. Zender, *J. Geophys. Res. Atmos.*, 2003, **108**, 4672, DOI: 10.1029/2002JD003143.
35 S. E. Bauer, Y. Balkanski, M. Schulz, D. A. Hauglustaine and F. Dentener, *J. Geophys. Res.-Atmos.*, 2004, **109**, art. no. D02304, DOI: 10.1029/2003JD003868.
36 F. Caloz, F. F. Fenter, K. D. Tabor and M. J. Rossi, *Rev. Sci. Instrum.*, 1997, **68**, 3172–3179.
37 S. Seisel, B. Fluckiger, F. Caloz and M. J. Rossi, *Phys. Chem. Chem. Phys.*, 1999, **1**, 2257–2266.
38 F. F. Fenter and M. J. Rossi, *J. Phys. Chem. A*, 1997, **101**, 4110–4113.
39 L. F. Keyser, S. B. Moore and M. T. Leu, *J. Phys. Chem.*, 1991, **95**, 5496–5502.
40 R. C. Sullivan, T. Thornberry and J. P. D. Abbatt, *Atmos. Chem. Phys.*, 2004, **4**, 1301–1310.
41 K. Tabor, L. Gutzwiller and M. J. Rossi, *J. Phys. Chem.*, 1994, **98**, 6172–6186.
42 I. Wangberg, T. Etzkorn, I. Barnes, U. Platt and K. H. Becker, *J. Phys. Chem. A*, 1997, **101**, 9694–9698.
43 L. A. Manucharova, S. V. Tsarukyan and I. A. Vardanyan, *Int. J. Chem. Kinet.*, 2004, **36**, 591–595.
44 D. W. Breck, *Zeolite Molecular Sieves*, Krieger Publishing Company, Dordrecht, 1984, pp. 593–724.
45 U. Brackmann, *Lambdachrome Laser Dyes (data sheets)*, Lambda Physik, Göttingen, 1996.
46 J. C. Miller and R. N. Compton, *J. Chem. Phys.*, 1981, **75**, 22–29.
47 R. M. Garnica, M. F. Appel, L. Eagan, J. R. McKeachie and T. Benter, *Anal. Chem.*, 2000, **72**, 5639–5646.
48 P. M. Johnson, M. R. Berman and D. Zakheim, *J. Chem. Phys.*, 1975, **62**, 2500–2502.
49 B. H. Rockney and E. R. Grant, *Chem. Phys. Lett.*, 1981, **79**, 15–18.
50 R. J. S. Morrison, B. H. Rockney and E. R. Grant, *J. Chem. Phys.*, 1981, **75**, 2643–2651.
51 P. M. Johnson, *Appl. Opt.*, 1980, **19**, 3920–3925.
52 P. Cremaschi, P. M. Johnson and J. L. Whitten, *J. Chem. Phys.*, 1978, **69**, 4341–4348.

